These data sharply contradict, and thus falsify the model. No escape by appeal to observational selection seems possible because the large-splitting, modest brightness ratio systems predicted by that model typically would be much easier to detect and recognize than those 27 that actually have been found. Could the observational selection effects and magnification bias not treated in this paper alter our conclusions? A recent treatment of this problem by Kochanek (*23*) carefully allowed for these effects (but did not perform the detailed numerical simulations we report here). From this work, we conclude that these effects [which were treated in an approximate fashion in our previous work (*2*)] would not alter our conclusions.

The failing of the model investigated is not presented as an entirely new result, but as a new and more robust manifestation of a previously recognized problem; namely, the excessively deep potential wells produced by the dark matter component in COBE-normalized standard CDM (*24–26*). These excessively deep potential wells lead to excess galactic pairwise velocity dispersions and to the predicted, excessive rate of large-splitting lensing events. The virtue of the lensing test is that it is independent of other tests and is not subject to the same caveats concerning bias of galaxies with respect to dark matter.

Are there variant models that would not fail these tests? Many alternative models have been considered or reconsidered in recent years. All of these add extra parameters such as allowance for a nonstandard spectrum shape, for other components of matter (such as massive neutrinos), or for less matter than is assumed in the flat ($\Omega = 1$) models. The simplest change that one can make in the standard scenario is to reduce the density of the clumped material in the universe, because the large number of large mass concentrations is what produces the overabundance of large splittings. Thus, a lower value of Ω clearly is useful (this also increases the computed age of the universe), but it would be premature to argue that our results by themselves indicate $\Omega < 1$, for many other properties of the scenario (such as temperature of the dark matter and shape of the power spectrum) contribute to lensing properties. However, the directness of gravitational lensing as a test for the growth of inhomogeneities, coupled with the rapidly increasing power of computers and numerical algorithms, makes us optimistic that calculations of the type about which we report here should become a major tool for testing and discriminating among competing cosmological scenarios.

REFERENCES AND NOTES

1. R. Narayan and S. D. M. White, *Mon. Not. R. Astron. Soc.* **231**, 97 (1988).
2. R. Cen, J. R. Gott, J. P. Ostriker, E. L. Turner, *Astrophys. J.* **423**, 1 (1994).
3. G. F. Smoot, *et al.*, *ibid.* **396**, L1 (1992).
4. G. Efstathiou, J. R. Bond, S. D. M. White, *Mon. Not. R. Astron. Soc.* **258**, 1 (1992).
5. E. Bertschinger and J. Gelb, *Astrophys. J.* **436**, 467 (1994).
6. E. L. Turner, J. P. Ostriker, J. R. Gott III, *ibid.* **284**, 1 (1984).
7. P. Schneider, J. Ehlers, E. E. Falco, *Gravitational Lensing* (Springer-Verlag, Berlin, 1992).
8. J. Wambsganss, thesis, Max-Planck-Institute for Physics and Astrophysics, Munich (1990).
9. B. Fort and Y. Mellier, *Astron. Astrophys. Rev.* **5**, 239 (1994).
10. E. L. Turner, *Astrophys. J.* **243**, L135 (1980).
11. R. Narayan and S. Wallington, in *Gravitational Lenses in the Universe*, J. Surdej *et al.*, Eds. (University of Liège, Liège, Belgium, 1993), p. 217.
12. P. Fischer, J. A. Tyson, G. M. Bernstein, P. Guhathakurta, *Astrophys. J.*, in press.
13. J. Surdej *et al.*, *Astron. J.* **105**, 2064 (1993).
14. D. Maoz *et al.*, *Astrophys. J.* **409**, 28 (1993).
15. H. K. C. Yee, A. V. Fillipenko, D. Tang, *Astron. J.* **105**, 7 (1993).
16. D. Crampton, R. D. McClure, J. M. Fletcher, *Astrophys. J.* **392**, 23 (1992).
17. A. R. Patnaik, I. W. Browne, D. Walsh, F. H. Chaffee, C. B. Folts, *Mon. Not. R. Astron. Soc.* **259**, 1 (1992).
18. J. N. Hewitt *et al.*, *Lect. Notes Phys.* **330**, 147 (1989).
19. J. Surdej and G. Soucail, *Proceedings of the 31st Liège International Astrophysical Colloquium* (University of Liège Liège, Belgium, 1993), p. 205.
20. D. Maoz and H.-W. Rix, *Astrophys. J.* **416**, 425 (1993).
21. C. S. Kochanek, *ibid.* **417**, 438 (1993); *ibid.* **419**, 12 (1993).
22. M. Fukugita and E. L. Turner, *Mon. Not. R. Astron. Soc.* **253**, 99 (1991).
23. C. S. Kochanek, Harvard-Smithsonian CfA preprint 3985 (1994).
24. M. Davis, G. Efstathiou, C. S. Frenk, S. D. M. White, *Nature* **356**, 489 (1992).
25. N. A. Bahcall and R. Cen, *Astrophys. J.* **398**, L81 (1992).
26. J. P. Ostriker, *Annu. Rev. Astron. Astrophys.* **31**, 689 (1993).

27. We thank J. R. Gott, C. S. Kochanek, and P. Schneider for useful discussions and the National Center for Supercomputing Applications for our use of the Convex-3880 supercomputer. We also gratefully acknowledge the financial support of NASA grants NAGW-2448 and NAGW-2173 and NSF grants AST92-08103 and HPCC ASC-9318185.

2 November 1994; accepted 31 January 1995

Imaging the Pore Structure of Geomaterials

J. T. Fredrich,* B. Menéndez,† T.-F. Wong

Laser scanning confocal microscopy can be used to image the pore structure of geologic materials in three dimensions at a resolution of 200 nanometers. The technique involves impregnation of the void space with an epoxy doped with a fluorochrome whose fluorescent wavelength matches the excitation wavelength. Optical sections with a thickness of less than 1 micrometer can be sliced from thick polished sections and combined to produce three-dimensional reconstructions. Application of the technique to rocks with porosities from 1 to 20 percent reveals the geometric complexity of the pore space. The technique can also be applied to other brittle solids such as ceramics.

The pore structure of rocks is both varied and complex: Crystalline rocks are dominated by microcracks (*1*), whereas sedimentary rocks typically contain voids in a variety of shapes, including nodal pores situated at grain vertices and sheetlike throats (microcracks) along two-grain boundaries (*2*). Physical rock properties such as permeability, electrical resistivity, seismic velocity, elastic moduli, and strength are affected not only by the porosity but also by the pore size distribution and connectivity (*3*). The compressive failure of rock involves damage accumulation (*4*), which significantly modifies the pore geometry.

Statistical descriptions of the pore space can be inferred indirectly from mercury injection, small-angle scattering, and adsorption analyses (*5*); however, direct observational methods permit quantification of diverse parameters including porosity, specific surface area, pore size and shape distribution, connectivity, surface roughness, and grain contact area. Conventional imaging technologies, such as optical light microscopy and scanning electron microscopy, rely on the analysis of polished planar sections. However, damage, in the form of widened cracks or pores and eradicated fine structure, may be induced during preparation and obscure analysis. Although ion milling has been proposed (*6*) to etch away the upper layer of damaged material, the technique is time consuming and problems can arise that are due to differential thinning rates in polymineralic rocks (*7*). A more important limitation (*8*) is that conventional techniques are confined to a two-dimensional (2D) view of a three-dimensional (3D) structure. Although pore casts can be prepared for qualitative study (*9*), destructive serial sectioning is necessary for quantitative characterization. Conventional serial sectioning techniques (*10*) are deficient in that

J. T. Fredrich, Geomechanics Department 6117, Sandia National Laboratories, Albuquerque, New Mexico 87185–0751, USA.
B. Menéndez and T.-F. Wong, Department of Earth and Space Sciences, State University of New York, Stony Brook, New York 11794–2100, USA.

*To whom correspondence should be addressed.
†Present address: Institut de Physique du Globe de Strasbourg, 67084 Strasbourg Cedex, France.

they are time consuming and tedious.

Laser scanning confocal microscopy (LSCM) has been used extensively in the biological sciences but has seen only limited application to nonbiologic (solid) materials (11). The theoretical conception dates back over 30 years to Minsky (12); however, routine application has only been made possible by recent advances in optical and electronic technology (13). In particular, interfacing of the microscope with a computer allows for precise control of both the lateral (x-y) coordinates of the laser and axial (z) position of the stage, and also enables automatic rapid processing as the laser is scanned across the field of view.

The essential feature of LSCM is that both illumination and detection are confined to a single location on the specimen at any one time. Because each point in the focal (image) plane is examined individually (in the absence of light scattered from neighboring points), in-plane (x-y) resolution is greatly enhanced, and resolution to ~200 nm is typically achieved. The confocal aperture admits light from only a specific plane of interest; thus, thin optical sections can be resolved by variation in the depth of the focal plane in the sample. The thickness of the optical section depends on both the opening of the confocal aperture and the particular objective lens; axial (z) resolution of <1 μm can be achieved with a relatively high magnification objective. Because the 2D images are originally obtained in digital form, a series of successive optical sections can be analyzed with commercially available image analysis software to create 3D reconstructions or perform complex measurements.

Our technique for visualizing the pore structure takes advantage of the weak natural fluorescence of most minerals. A dry plug of the rock sample is evacuated and immersed in an ultra–low-viscosity slow-curing epoxy doped with a suitable fluorochrome (14) while still under vacuum. After the epoxy has degassed, the vacuum is released and the epoxy is consequently forced into the interconnected void space of the rock. For relatively impermeable rocks, a pressure (~10 MPa) is applied before vacuum release (15). After curing, the plug is sectioned to a thickness of ~0.5 to 1 mm, and the resultant planar section is polished by means of standard abrasive techniques. Laser illumination of the exposed surface of the thick section causes fluorescence of the epoxy and, because most minerals are not fluorescent, an unobstructed image of the pore structure is rendered.

The dimension of the pore space typically scales with the grain size, and the ability to section serially to a depth of one to two grain sizes is thus desirable. Penetration of the laser into geologic samples is limited by the opacity of most minerals; however, this can be somewhat compensated for because geologic samples can, if necessary, be illuminated at full laser intensity, whereas imaging of delicate biologic samples usually requires filtering to just a few percent of the original laser power.

We successfully imaged the pore structure of various rocks (16), including several sandstones with porosities ϕ ranging from 4 to 20%, limestone (ϕ ~12%), and low-porosity (ϕ ~1%) marble, granite, and dunite. Serial sectioning can, in many cases, be done to depths in excess of ~150 μm (0.15 mm), which is of the order of the grain size for many rocks of interest.

As an application of the technique to the analysis of transport properties, we imaged a pure quartz sandstone (Fontainebleau) with a highly variable porosity resulting from differing degrees of cementation during diagenesis. The reconstructions show that dramatic changes in pore size and connectivity occur with cementation. In the weakly cemented

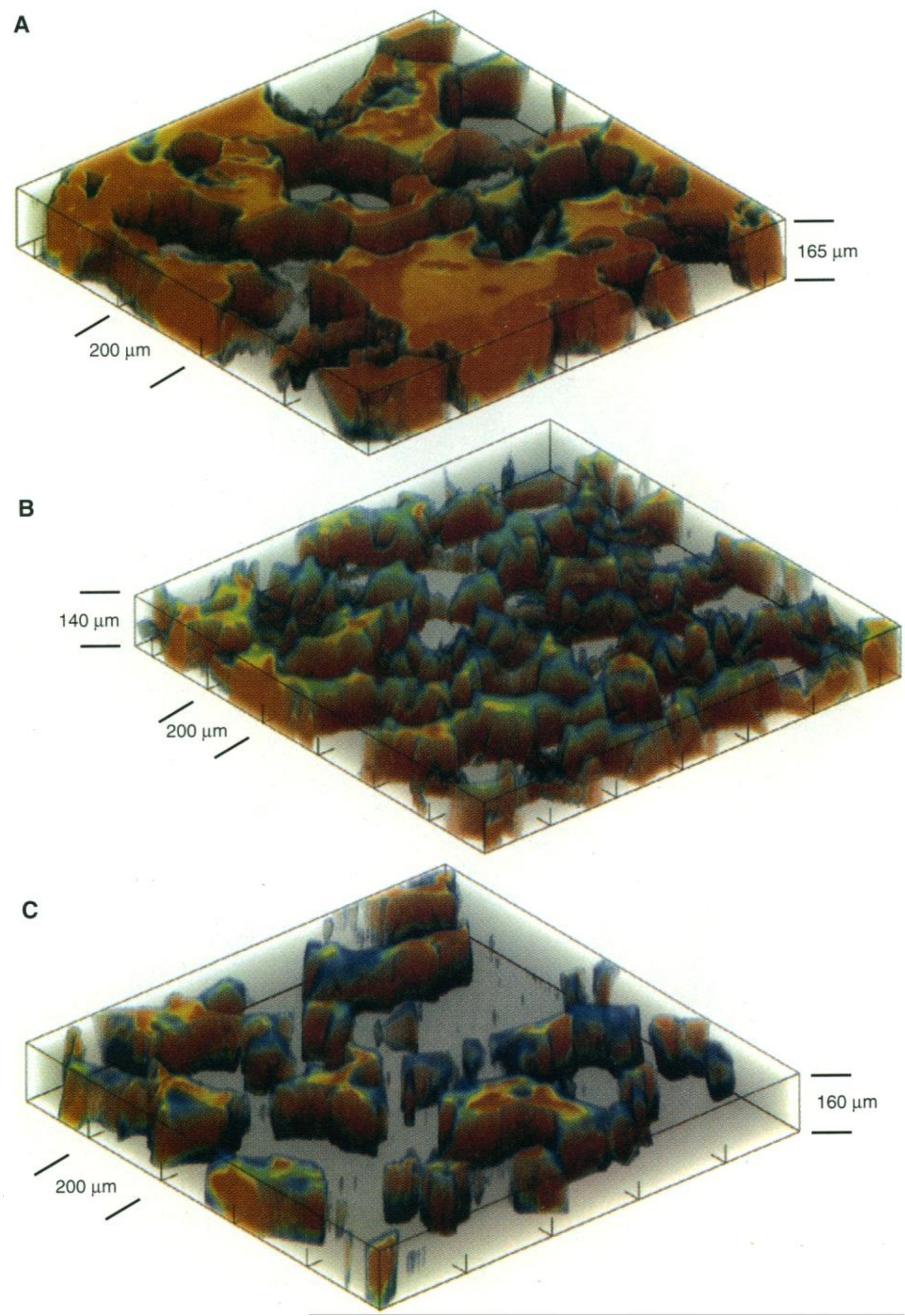

Fig. 1. Three-dimensional reconstructions of the pore space of a quartz sandstone with an average grain size of ~250 μm. The pore space is opaque (colored) and the solid matrix is translucent. (**A** and **B**) For weakly to moderately cemented samples, systematic decreases in hydraulic permeability appear to result from reduced pore sizes with no changes in connectivity. (**C**) Accelerated permeability reduction for strongly cemented samples appears to result from a pronounced loss in connectivity.

sample with ϕ = 20% (Fig. 1A), the pore space is made up of a complex network of equidimensional nodal pores and sheetlike cracks that are highly interconnected. Pore sizes, as characterized by stereological measurement of chord lengths, range from <10 to 250 μm across, and about 30% are <10 μm across (*17*). At ϕ = 10% (Fig. 1B), pore sizes are significantly smaller so that more than 50% of the chords are less than 10 μm; however, the pore space remains highly interconnected. In contrast, sheetlike cracks linking nodal pores in the highly cemented sample with ϕ = 4% (Fig. 1C) are less common, implying a significant loss of connectivity.

Laboratory measurements on Fontainebleau sandstone have shown that reduction in hydraulic permeability is accelerated as porosity is reduced below 9% (*17*). The reconstructions suggest that permeability reduction in the weakly to moderately cemented samples ($\phi \geq 10\%$) was primarily a result of an overall decrease in pore size without a significant change in connectivity. However, connectivity loss dominated in the highly cemented samples ($\phi < 9\%$). In accordance with percolation theory (*18*), a drastic decrease in permeability occurred as the percolation threshold was approached, with the development of increasing numbers of isolated clusters and, ultimately, a complete loss of connectivity.

Another example of the application of LSCM is in the study of brittle failure processes and stress-induced damage evolution in low-porosity ($\phi \sim 1\%$) crystalline rock. 3D reconstructions of unstressed Westerly granite (Fig. 2A) reveal that the pore space is interconnected and made up of equidimensional pores and relatively thin and elongated microcracks, which probably resulted from cooling and depressurization during uplift. This particular reconstruction reveals in detail the nonplanar geometries of a partially cracked grain boundary and a bifurcated intragranular crack. The crack aperture and surface roughness, which influence both the elastic moduli and seismic velocity, are highly variable. The uncracked parts of the grain boundary may represent geometric barriers at which cracking was arrested or localized regions that experienced crack healing.

Under compressive loading, preexisting cracks can propagate farther and new cracks may initiate, as shown for a triaxially compressed dunite (Spruce Pine) in Fig. 2B. The stable growth of a multiplicity of such cracks results in a net increase in volume (dilatancy) and enhanced hydraulic permeability. Although damage accumulation results in a complex pore geometry, there is a clear preference for the cracks to propagate along a path subparallel to the maximum (compressive) principal stress σ_1, as predicted by fracture mechanics. The failure mode in this dunite, which contains a grain boundary–lining ductile phase (serpentine), was pressure dependent. Samples deformed at lower pressures failed because of coalescence of microcracks and shear localization, whereas at higher pressures, intragranular cracks were arrested at grain boundaries, with extensive delamination of grain boundaries (*19*). Consequently, transgranular propagation and coalescence of microcracks were inhibited, and the rock deformed by homogeneously distributed microcracking (cataclastic flow) with no loss in load-bearing capacity.

Other geologic applications include measurement of preferred crack orientation for interpretation of in situ stress directions or evaluation of coring-induced damage. This technique can likewise be applied to the study of micromechanical processes in other brittle materials, such as evolution of pore geometry during sintering of ceramics and damage in microelectronic components.

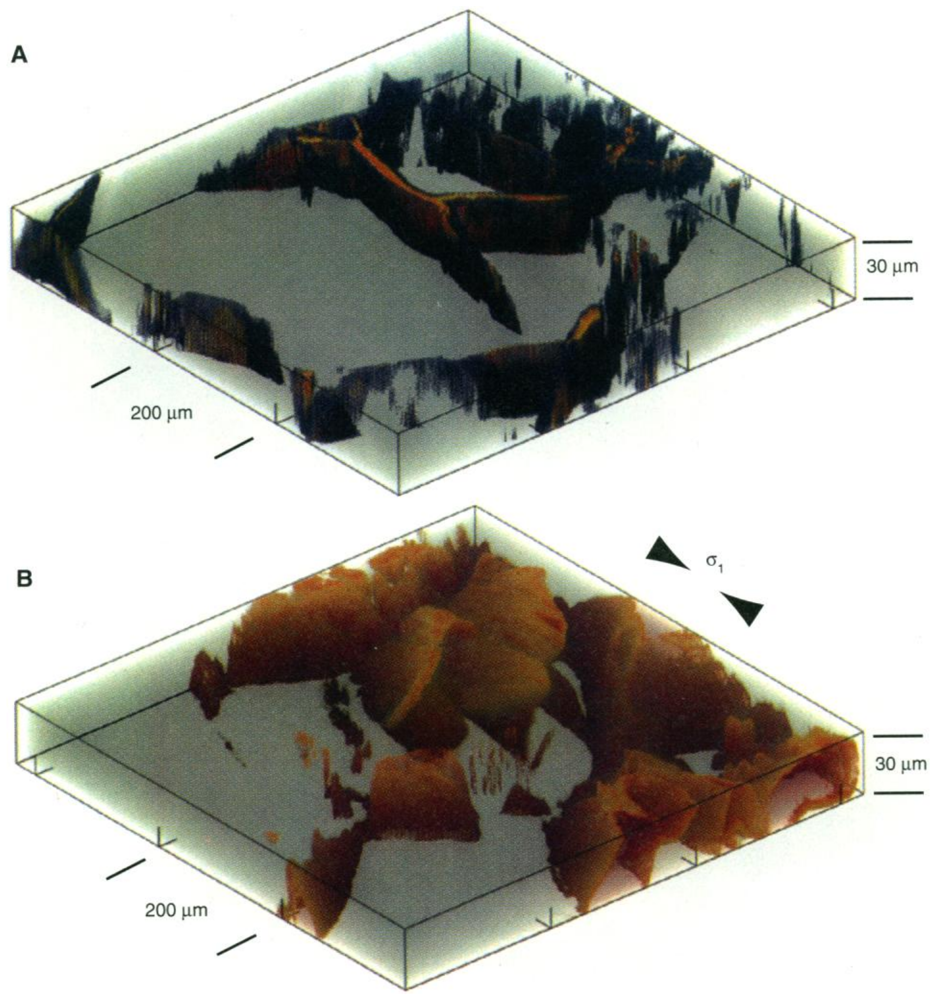

Fig. 2. Three-dimensional reconstructions of the pore space of low-porosity crystalline rocks. **(A)** Unstressed Westerly granite. A partially cracked grain boundary curves around the two edges in the foreground and a doubly bifurcated intragranular crack traverses part of the grain. **(B)** Triaxially compressed sample of dunite loaded in compression at a confining pressure of 250 MPa in the transitional regime between strain softening and stable work-hardening behavior. A complex array of closely spaced intragranular cracks impinge on a grain boundary at the near right edge, and a complex array of intragranular cracks is visible in the rear half.

REFERENCES AND NOTES

1. R. L. Kranz, *Tectonophysics* **100**, 449 (1983).
2. F. A. L. Dullien, *Porous Media, Fluid Transport and Pore Structure* (Academic Press, New York, ed. 2, 1992).
3. Y. Guéguen and V. Palciauskas, *Introduction to the Physics of Rocks* (Princeton Univ. Press, Princeton, NJ, 1994).
4. M. S. Paterson, *Experimental Rock Deformation—The Brittle Field* (Springer-Verlag, New York, 1978).
5. J. Van Brakel, S. Modry, M. Svata, *Powder Technol.* **29**, 1 (1981); P.-Z. Wong, J. Howard, J.-S. Lin, *Phys. Rev. Lett.* **57**, 637 (1986); D. Avnir, D. Farin, P. Peifer, *J. Colloid Interface Sci.* **103**, 112 (1984).
6. W. F. Brace, E. Silver, K. Hadley, C. Goetze, *Science* **278**, 162 (1972).
7. J. T. Fredrich and T.-F. Wong, *J. Geophys. Res.* **91**, 12743 (1986).
8. C. Lin and M. H. Cohen, *J. Appl. Phys.* **53**, 4152 (1982); Y. Bernabe, *Geophysics* **56**, 436 (1991).
9. E. D. Pittman and R. W. Duschatko, *J. Sediment. Petrol.* **40**, 2253 (1970); L. J. Pyrak-Nolte and C. M. Montemagno, in *Rock Mechanics*, P. P. Nelson and

S. E. Laubach, Eds. (Balkema, Rotterdam, Netherlands, 1994), pp. 81–88.
10. J. Koplik, C. Lin, M. Vermette, *J. Appl. Phys.* **56**, 3127 (1984).
11. T. Kobayashi and D. A. Shockey, *Adv. Mater. Proc.* **140**, 28 (November 1991) and 24 (December 1991); *Trans. Soc. Prof. Well Log Anal.*, Thirty-third Annual Logging Symp. Paper No. 9926, Oklahoma City, OK, 14 to 17 June 1992 (Soc. Prof. Well Log Anal., Houston, TX, 1992).
12. M. Minsky, U.S. Patent 3,013,467.
13. J. B. Pawley, Ed., *Handbook of Biological Confocal Microscopy* (Plenum, New York, 1990).
14. The choice of fluorochrome is critical because the fluorescent wavelength λ_2 of the fluorochrome must closely match the excitation wavelength λ_1. Sectioning ability is optimized for $\beta = \lambda_2/\lambda_1 = 1$ (analogous to the case for a perfect reflector), and in the limit $\beta \rightarrow \infty$, the LSCM loses its sectioning ability altogether and the resultant image is equivalent to that obtained with conventional microscopy (*13*).
15. B. Menéndez Villar, thesis, University of Oviedo, Oviedo, Spain (1992).
16. We used a Bio-Rad MRC-600 Confocal Imaging System attached to the side port of an inverted optical microscope (Nikon Diaphot). A krypton-argon laser (15 mW) was used as a light source, with a 568-nm excitor filter and YHS (rhodamine) filter block. The epoxy was doped with rhodamine B (C.I. 45170) and penetration of epoxy into cracks with apertures at the resolution limit ($\sim$200 nm) was verified directly. The 3D reconstructions were made with the use of VoxelView/Ultra2.1 (Vital Images, Fairfield, IA) on a Silicon Graphics XS24 workstation.
17. T. Bourbie and B. Zinszner, *J. Geophys. Res.* **90**, 11524 (1985); J. T. Fredrich, K. H. Greaves, J. W. Martin, *Int. J. Rock Mech. Min. Sci. Geomech. Abstr.* **30**, 691 (1993). Analogous results for hot-pressed quartz and calcite are discussed by W. Zhu, C. David, and T.-F. Wong (in preparation).
18. D. Stauffer and A. Aharony, *Introduction to Percolation Theory* (Taylor and Francis, Philadelphia, PA, 1992).
19. Additional information about the experimental results and micromechanical behavior is provided by J. T. Fredrich and T.-F. Wong (in preparation).
20. We thank M. W. Folsom, D. J. Holcomb, E. J. King, and A. Rodríguez Rey for discussions. S. Stricker provided access to facilities at the University of New Mexico. Funding from the Office of Basic Energy Sciences (Geosciences Program), U.S. Department of Energy (DOE), is gratefully acknowledged. Portions of this work were done at Sandia National Laboratories, supported by DOE under contract DE-AC04-94AL85000. B.M. was supported at State University of New York, Stony Brook, by a postdoctoral fellowship from Fundacion para el Fomonto en Asturias de la Investigacion Cientifica Aplicada y la Tecnologia, Asturias, Spain.

23 November 1994; accepted 31 January 1995

A Modular Steel Freeway Bridge: Design Concept and Earthquake Resistance

W. H. Wattenburg, D. B. McCallen, R. C. Murray

A modular multilane steel freeway bridge has been constructed from surplus railroad flatcar decks. It can be erected on-site in a few days' time. It has been built and static-load tested for emergency freeway bridge repair. This inexpensive modular bridge may also have broad application around the world for low-cost bridges in areas where funds are limited. On the basis of static-load testing performed by the California Department of Transportation and computer dynamic analysis, this simple modular-design concept has the potential of providing a strong bridge that can withstand the severe aftershocks expected immediately after a major earthquake.

A modular steel, multilane freeway bridge was constructed and evaluated in March 1994 by the California Department of Transportation (Caltrans) as a temporary bridge for emergency freeway repair. It can be erected on-site within a few days' time without extensive site preparation or ground disturbance to restore traffic over damaged freeway sections such as those that collapsed in the 1994 Northridge earthquake and the recent Hyogo-Ken Nanbu earthquake in Japan. Because of its potential importance for emergency response and other infrastructure uses described herein, we independently performed a computer dynamic analysis of a model of the bridge at the Lawrence Livermore National Laboratory to investigate its earthquake response characteristics.

The modular bridge design was first proposed by Wattenburg (*1*) and constructed by Caltrans (Fig. 1). The as-built modular bridge uses only one standard structural module: inexpensive surplus railroad flatcar decks. However, structurally equivalent modules can be constructed from ordinary steel I-beams. This design has its own base support for the column structures (bents) and requires only simple steel fasteners. This modular bridge costs relatively little compared to other steel and reinforced or prestressed concrete freeway bridges, which cost three to five times as much and require months to construct.

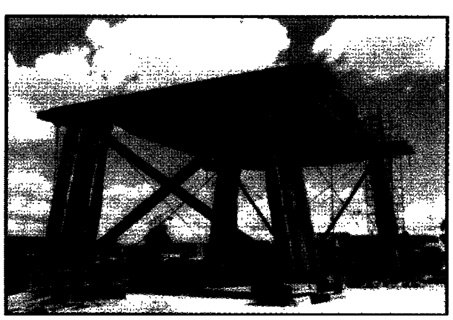

Fig. 1. Prototype module constructed for the California Department of Transportation.

The modular bridge constructed by Caltrans is shown in Fig. 2. The individual 3 m wide by 16 m long flatcar modules (Fig. 2A) are massive steel frame structures that are designed to carry loads of up to 50 metric tons. The flatcar modules are coupled together in interlocked fashion such that the module connections emulate pinned joints (Fig. 2B). The 15-m-wide roadway deck of the assembled bridge consists of four flatcars side-by-side, which span 16 m between two vertical piers (Fig. 2C). The piers are constructed with a single flatcar in the horizontal direction (on top) supported by two half-flatcar vertical columns. The pier structure provides its own foundation with a horizontally placed flatcar on the ground at the foot of each pier. In the transverse direction, two diagonal steel braces are added to provide stability and stiffness to the assembled pier structure. Strong surplus boxcar center beams are used for the diagonal braces. In the longitudinal direction, the underside of the bridge is left open without obstruction to allow for passage of traffic from cross streets or railroads spanned by the bridge.

Vertical steel cables are used to constrain the top and bottom horizontal modules of the piers so that the vertical columns between them cannot come out of their joint sockets in the horizontal modules. The four adjoining flatcars on the top, which form the bridge roadway, are coupled together side-by-side by inserting simple U-bolt brackets into matching stake slots on the side of each flatcar deck (Fig. 2).

Ten surplus railroad flatcars were required for the bridge shown in Fig. 1. The Caltrans prototype was erected in 10 days by a construction crew of four, utilizing one 22.7–metric ton–capacity crane. The interconnection of the flatcars was accomplished in "Lego-block" fashion (*2*) to minimize the need for special brackets and to reduce assembly time. The ends of the vertical column flatcar modules are cut in a configuration such that their beam ends project into and around the support beams of the horizontal modules above and below.

Caltrans tested the as-built modular bridge with a static load of $\sim$110 metric tons at center span. The observed vertical deflection was only $\sim$0.3 cm under this heavy loading. We decided to analyze the stand-alone, 16-m-long bridge section shown in Fig. 1 for its ability to withstand significant seismic ground motion, in par-

W. H. Wattenburg, University Foundation, California State University, Chico, CA 95929, USA.
D. B. McCallen, Structural Mechanics Group, Lawrence Livermore National Laboratory, Livermore, CA 94550, USA.
R. C. Murray, Geologic and Atmospheric Hazards, Lawrence Livermore National Laboratory, Livermore, CA 94550, USA.